Optical Quality Resorbable Calcium-Phosphate Glasses for Biophotonic Applications

Original
Optical Quality Resorbable Calcium-Phosphate Glasses for Biophotonic Applications / Pugliese, D., Boetti, N.G., Janner, D., Milanese, D. (POLITO SPRINGER SERIES). - In: Ceramics, Glass and Glass-Ceramics From Early Manufacturing Steps Towards Modern Frontiers / Baino F., Tomalino M., Tulyaganov D.. - ELETTRONICO. - [s.l] : Springer, 2021. - ISBN 978-3-030-85775-2. - pp. 229-252 [10.1007/978-3-030-85776-9_7]

Publisher:
Springer

Published
DOI:10.1007/978-3-030-85776-9_7

Optical quality resorbable calcium-phosphate glasses for biophotonic applications

Diego Pugliese[1][0000-0002-6431-1655], Nadia Giovanna Boetti[2][0000-0002-5269-2390], Davide Janner[1][0000-0001-7954-979X] and Daniel Milanese[3][0000-0002-6257-3600]

[1] DISAT - Politecnico di Torino and RU INSTM, Torino 10129, Italy
[2] LINKS Foundation - Leading Innovation and Knowledge for Society, Torino 10138, Italy
[3] DIA - Università di Parma and RU INSTM, Parma 43124, Italy
diego.pugliese@polito.it

Abstract. Recently developed calcium-phosphate glass formulations are proposed in this chapter as a new class of materials for biomedical optics and photonics. The glasses have been designed and carefully prepared in our laboratory to be dissolvable in biological fluids while being optically transparent, mechanically reliable both in dry and humid environments, and suitable for both preform extrusion and fiber drawing. Optical fibers have been drawn from these glasses using our custom-made induction heated drawing tower and showed attenuation loss values from one to two orders of magnitude lower than the counterpart polymeric-based bioresorbable devices reported in literature. In addition, the optical fibers have been implanted in living rats for several weeks and no clinical signs of any adverse effect have been found. Results on the inscription and characterization of different types of fiber Bragg grating-based optical filters will be also shown, together with the demonstration of the suitability of the above-mentioned bioresorbable optical fibers for time-domain diffuse optical spectroscopy.

Keywords: Calcium-phosphate Glass, Bioresorbable Optical Fiber, In-vivo Testing, Extrusion, Fiber Bragg Grating, Time-domain Diffuse Optics.

1 Introduction

Among oxide glasses, phosphate glasses have attracted an increasing interest in the scientific community, thanks to the specific functionalities provided by proper design of their composition.

Initially phosphate glasses were studied thanks to their ability to resist to hydrofluoric acid and for other applications, such as incorporation of radioactive wastes [1, 2]. Further interest for phosphate glasses arose due to their high transparency in the Ultraviolet (UV) wavelength range [3] and for the development of near-infrared wavelength high power lasers [4], and optical fiber-based lasers and amplifiers [4–6].

More recently, suitable engineering of the composition of phosphate glasses allowed obtaining dissolution in aqueous media, opening the way toward the realization of resorbable materials for their use in biomedicine [7]. The base composition includes calcium and sodium oxides as network modifiers and was exploited to develop fibers to be used as fillers for biopolymers to obtain a resorbable composite for bone repair [8]. Fiber drawing of calcium-phosphate glasses could lead to the realization of scaffolds which played a key role in neuronal polarization and axonal growth direction [9].

In this chapter, the fabrication and characterization of a phosphate glass composition able to combine resorbability with high optical quality is reported. This formulation was engineered based on previous recipes in order to fabricate specialty optical fibers suitable for biophotonic applications, which range from fiber Bragg grating biosensors to diffuse optics and measurement of pH.

2 Phosphate glass optical fibers

2.1 Phosphate glass synthesis and characterization

Phosphate glasses were based on the composition (in mol%) 50 P_2O_5 − (30 - x) CaO − (3 + x) MgO − 11.5 Na_2O − 2.5 B_2O_3 − 3 SiO_2, with x = 0, 5, 12, 20. The glasses were fabricated by melting chemicals of high purity level (99+%) in alumina crucibles inside a chamber furnace at the temperature of 1200 °C for 1 h, followed by casting into preheated brass molds [10]. Subsequently, the glasses were annealed at a temperature around the glass transition temperature, T_g, for 5 h to relieve internal stresses, and finally cooled down slowly to room temperature.

Differential thermal analysis (DTA) was performed using a Netzsch DTA 404 PC Eos differential thermal analyzer up to 1200 °C with a heating rate of 5 °C/min in sealed Pt/Rh pans.

Density of the glasses was measured at room temperature by the Archimedes' method using distilled water as immersion fluid, while coefficient of thermal expansion (CTE) was measured by dilatometry using a Netzsch DIL 402 PC horizontal alumina dilatometer operating at 5 °C/min on 5 mm-long specimens.

The values of density, T_g, onset crystallization temperature (T_x), and CTE of the prepared glasses are reported in Table 1.

Table 1. Physical and thermal properties of the synthesized calcium-phosphate glasses.

Glass name	MgO [mol%]	Density ± 0.005 [g/cm^3]	T_g ± 3 [°C]	T_x ± 3 [°C]	CTE ± 0.1 [10^{-6} °C^{-1}]
G1	3	2.606	435	658	12.6
G2	8	2.600	435	628	12.2
G3	15	2.598	442	632	12.0
G4	23	2.589	444	625	12.2

The specimens were cut and polished to an optical quality for optical and spectroscopic characterization, in order to assess the possible matching of two of the prepared glasses to constitute the core and cladding components of an optical fiber.

The refractive index (R.I.) of the glasses was measured by means of the prism coupling technique, using a Metricon Model 2010, at the wavelengths of 633, 825, 1061, 1312, and 1533 nm. Ultraviolet-Visible/Near-infrared (UV-Vis/NIR) spectroscopy was carried out with a Varian Cary 500 spectrometer in the wavelength range between 190 and 3000 nm.

As an example, Fig. 1 shows the transmittance of the G1 glass as a function of the wavelength. The inset reports the refractive index values of all the prepared glasses at the wavelength of 633 nm.

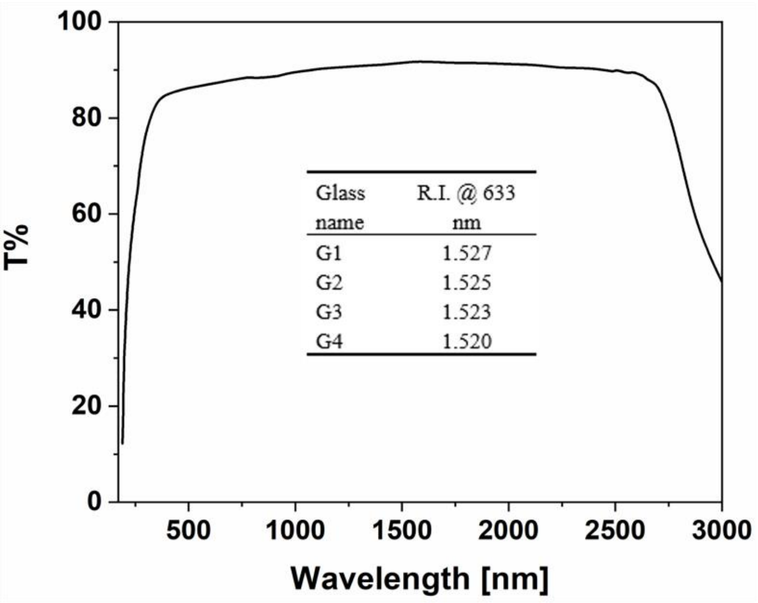

Glass name	R.I. @ 633 nm
G1	1.527
G2	1.525
G3	1.523
G4	1.520

Fig. 1. Transmittance spectrum of G1 glass; the inset reports the refractive index values of all the synthesized calcium-phosphate glasses at 633 nm.

From Fig. 1, it is clearly possible to observe that G1 glass shows a noticeably broad transparency window from the NIR down to the near UV, while the refractive index values appear to decrease linearly with increasing MgO molar content in substitution to CaO in the composition of the glass [10].

Degradation tests were carried out on 150 ± 6 µm diameter single-material fibers of the four different glass compositions, drawn using an in-house developed induction heated drawing tower and subsequently soaked in phosphate buffered saline solution (PBS, pH = 7.4) at a temperature of 37 °C for 21 days. The solution volume to sample exposed area ratio was kept fixed to 0.1 ml/mm^2, and the refreshing of the medium was performed twice a week to simulate physiological fluid exchange.

The decrease in diameter of the G1, G2, G3, and G4 fibers was periodically monitored over the whole dissolution time (see Fig. 2). Overall, the results show a complete dissolution within 30 days in PBS for the G1 and G2 compositions, while G3 and G4 exhibited slower dissolution rates. However, it is of high interest observing how the dissolution kinetics can be tailored by modifying the glass composition. In particular, a decrease in glass solubility occurred when replacing MgO with CaO, thus indicating a higher strengthening effect of MgO with respect to CaO in the glass network [10].

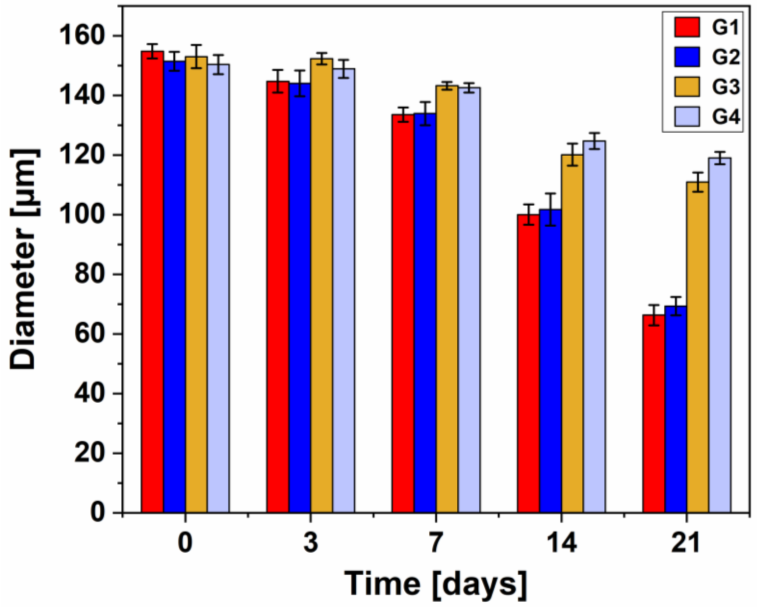

Fig. 2. Diameter values of the prepared glass fibers after 3, 7, 14, and 21 days of soaking in PBS solution.

2.2 Preform fabrication

In the development of the optical fibers, suitable glass pairs were selected. In the following paragraphs, details of the prepared optical fibers will include the selected glass pairs which suited best the requirements of the applications.

Glasses constituting the core of the optical fibers were shaped into rods by casting the melt into a pre-heated cylindrical mold. The so-obtained samples were polished to an optical quality using SiC disks of different grains. The cladding glass tubes were realized by means of extrusion or rotational casting techniques aiming at a central hole large enough to fit the core rod. Examples of core glass rod and cladding glass tubes constituting the optical fibers are reported in Fig. 3. The extrusion of the cladding preform is a very convenient process compared with other techniques such as rotational casting and allows to fabricate even very complex preforms [11].

The results obtained for rotational casting and extrusion of the bioresorbable phosphate glass cladding are compared in Fig. 3. It can be clearly observed that the surface of the preform obtained with rotational casting needs polishing to be used for fiber drawing. The surface of the extruded tube, instead, is readily usable for fiber drawing since it shows a smooth and even surface. With such technique there are no limitations given by the rotation speed, that restricts the achievable ratio between the outer and the inner diameter of the tube being at most 2:1. Indeed, with extrusion thin wall capillaries can be easily obtained achieving a ratio of outer to inner diameter ranging between 10:1 to 10:9. For the sake of completeness, it must be said that the main disadvantage of the extrusion process is the presence of a deformed initial and final part that must be cut off prior to the insertion of the core rod into the cladding tube. This fact leads to a reduction in the used material even though the discarded material can be remelted in future batches.

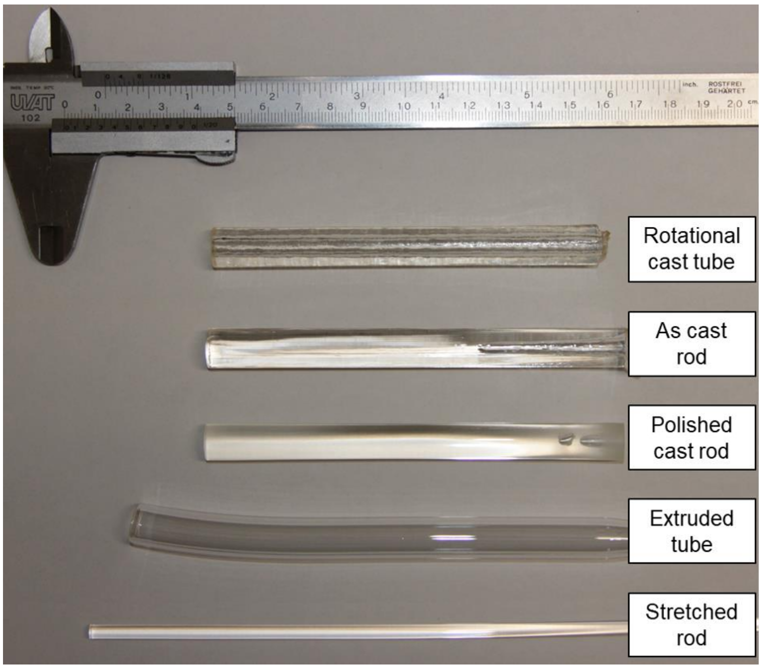

Fig. 3. Examples of core and cladding glass preforms used for the fabrication of the optical fibers: rotational casting cladding tube, as-cast and polished core rod, extruded cladding tube, and stretched core rod.

2.3 Optical fiber fabrication

The bioresorbable optical fibers can be fabricated in different configurations, however for the main applications as light guides the most common is the single core/cladding optical fiber. The preform, assembled as previously described, is fed into a drawing tower system that is reported in Fig. 4. The preform is progressively introduced into a susceptor under controlled nitrogen atmosphere with a radio frequency (RF) induction heating system (SAET, Torino, Italy) that can reach up to 800 ºC. After reaching the drawing temperature, the preform starts forming a neck and starts the drawing process under its own weight. After reaching the winding drum at the bottom of the drawing tower, the fiber is attached to it and is rolled onto the drum upon drawing. The feed rate of the preform and the rotation speed of the winding drum determine and control the diameter of the fiber, and for this reason are used as process parameters.

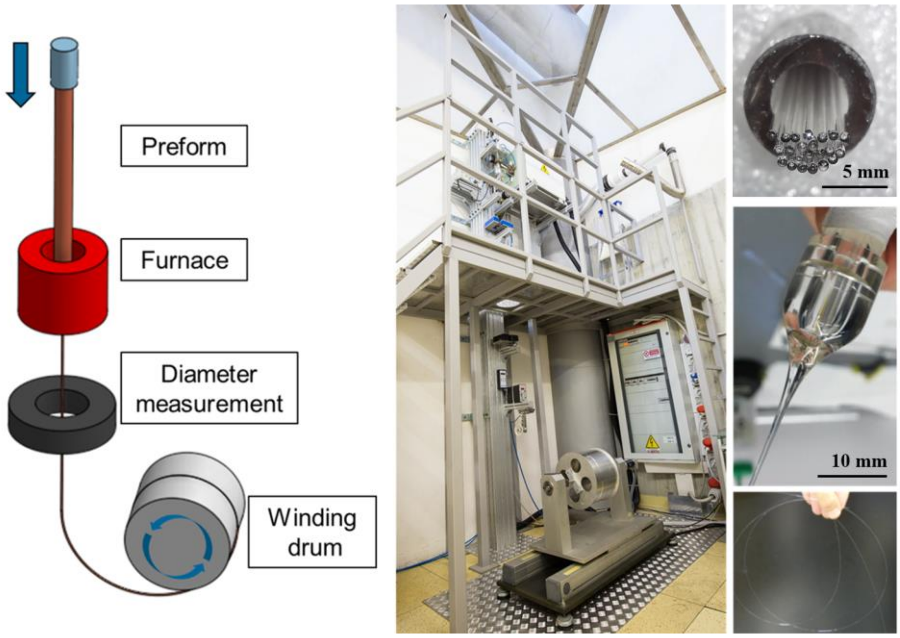

Fig. 4. Left panel: schematic illustration of a fiber drawing tower. Middle panel: optical fiber drawing tower located at Politecnico di Torino-LINKS. The preform is fed into a heated susceptor that brings it to the drawing temperature producing a fiber of controllable diameter. Right panel (from top to bottom): microstructured calcium-phosphate glass optical fiber preform, typical neck-down region of the optical fiber preform after the drawing process, example of optical fiber specimen.

The drawing process allowed to produce different types of fibers from multi-mode to single-mode. For biological applications, both these types are of great interest since they can be used for imaging or greater collection of light in the case of multi-mode fibers or for critical signal processing for spectroscopy in the case of single-mode ones. A typical example of bioresorbable multi-mode and single-mode fibers is reported in Fig. 5. Their cross-sectional view shows a very good core/cladding interface and a circular and centered core.

After fiber fabrication, a full optical and mechanical characterization has been performed to verify if the requirements for potential biomedical applications could be met.

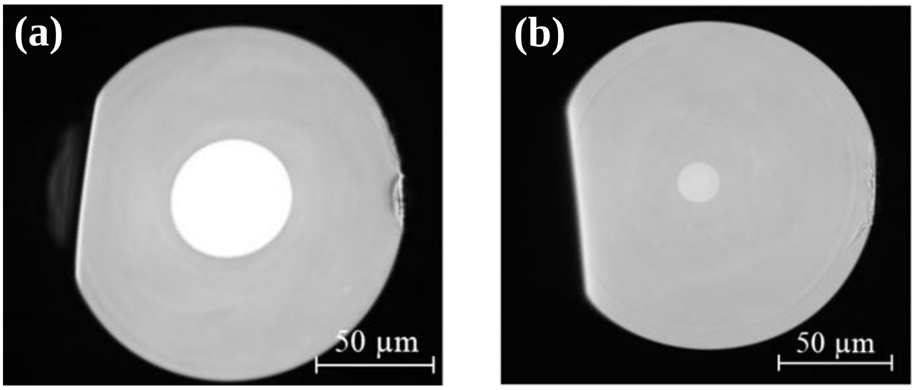

Fig. 5. Cross-sectional view of the drawn bioresorbable fibers showing a multi-mode (a) and a single-mode (b) configuration. Adapted from [10] under the Creative Common license CC BY and from [12].

2.4 Characterization of the prepared optical fibers

The two main requirements for the application of optical fibers in a biomedical context are centered around their mechanical strength and optical transmission properties. Indeed, a certain mechanical strength is required to withstand the possible stresses that might be generated by handling or implantation in the case of bioresorbable fibers. At the same time, a desired property is a reduced loss in light propagation and possibility to convey light in a part of the spectrum that is useful for e.g. fluorescence or diffusion spectroscopy.

The fabricated fibers were submitted to mechanical tensile tests as reported in Fig. 6 and adapted from [13]. The figure shows typical values of $\Delta L/F$ *vs.* L_0/A, from which an estimation of the elastic modulus of 48 GPa can be derived. Such value is in line with the original glass materials and implies a good rigidity of the fibers in a scenario of implantation inside the body, thus opening new interesting possibilities.

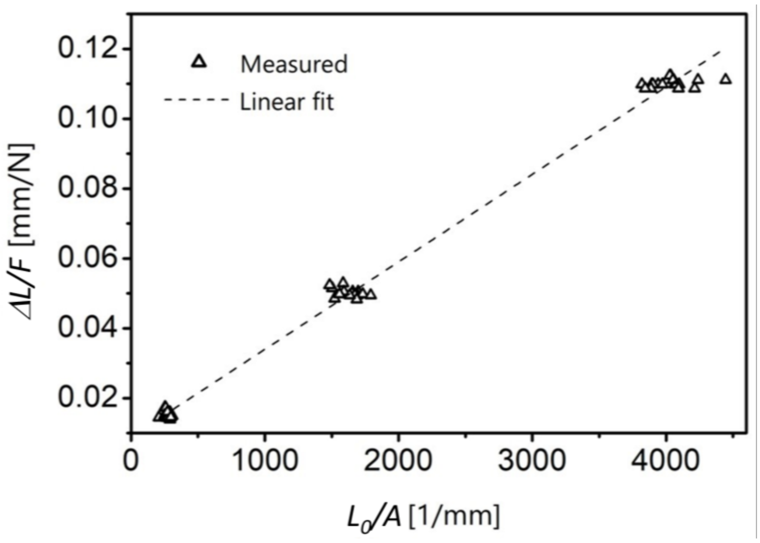

Fig. 6. A typical *ΔL/F vs. L_0/A* diagram for the bioresorbable optical fiber. The fitting line used for the elastic modulus estimate is also shown. Adapted from [13]. Copyright 2019, with permission from Elsevier.

Further characterization was performed to evaluate the optical properties of the bioresorbable optical fibers [10]. In this case, the tests were carried out at two distinct wavelengths: 633 and 1300 nm. The optical loss measurement of the single-mode fiber obtained via the cut-back method is reported in Fig. 7. As can be seen, the losses are 1.9 (4.7) dB/m at 1300 (633) nm, which are low values and very close to the estimated intrinsic absorption of the calcium-phosphate glass used for the fabrication.

The mechanical and optical properties make the produced fiber a very promising candidate for *in-vivo* biomedical applications both in a scenario of intravital monitoring or body implantation for theranostics purposes. Before reviewing the different applications, a thourough characterization of the *in-vivo* bioresorbability properties will be detailed in the next Section.

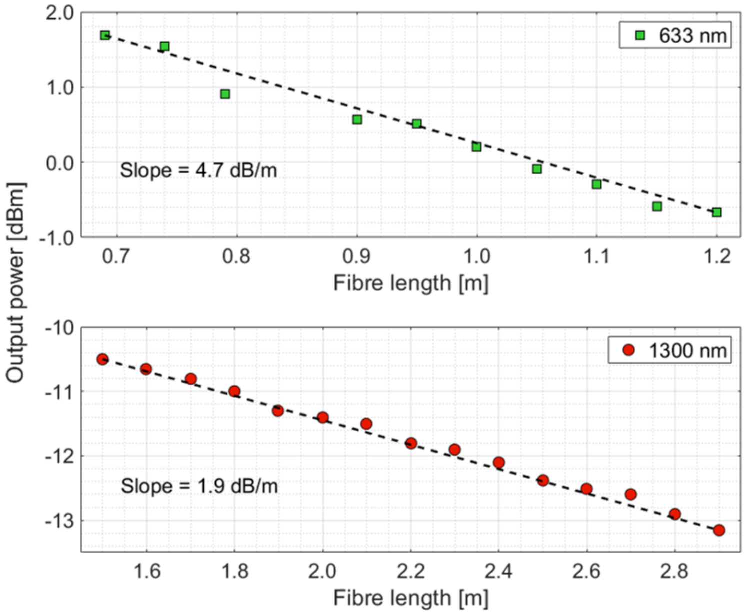

Fig. 7. Typical optical losses at 633 and 1300 nm of a single-mode bioresorbable optical fiber measured with the cut-back method. The square and circular symbols are the experimental points, while the dashed lines are the linear fitting curves. Adapted from [10] under the Creative Common license CC BY.

2.5 *In-vivo* tests of the biodegradable optical fibers

To assess the viability of the usage of the bioresorbable optical fibers, the response to implantation has been checked through *in-vivo* tests [14]. The latters were performed on adult male rats in the animal facility of the University of Defense, Faculty of Military Health Sciences and in the laboratories of the Biomedical Research Center, University Hospital in Hradec Králové. The administration of the phosphate fibers was realized by subcutaneous implantation of 1 cm-long phosphate fiber bundles to evaluate their biodegradability and potential toxicology risk. The bundle was secured by two knots of surgical thread as can be seen in Fig. 8a.

Control (CTRL) animals underwent the same operation without the administration of fibers. Tissue sampling was performed 2, 4 and 5 weeks after fibers administration and histopathological tissues analysis, biochemical and hematological analysis of blood were performed. The implanted fiber bundle extracted after 4 weeks and its microphotograph are shown in Figs. 8b and 8c, respectively. The postmortem examination included the site of implantation, external surfaces of the body, all orifices of the body and the cranial, thoracic, abdominal and pelvic cavities and their contents.

The blood tests were realized for eight parameters, namely urea, creatinine, sodium, potassium, chlorides, alanine aminotransferase, aspartate aminotransferase and C-reactive protein (CRP). Histological slides were prepared by common paraffin technique and stained with hematoxylin and eosin. One-way analysis of variance

(ANOVA) and Kruskal-Wallis test with Dunn's multiple comparison test were selected for statistical evaluation of the blood tests. The skin from the implantation site was histopathologically evaluated on day 14, day 28 and day 35.

As confirmed in the Table of Fig. 8d, no clinical signs of adverse reactions were found in tested animals after implantation of the bioresorbable fibers. Indeed, the CRP, whose levels rise in response to an inflammation, showed normal values.

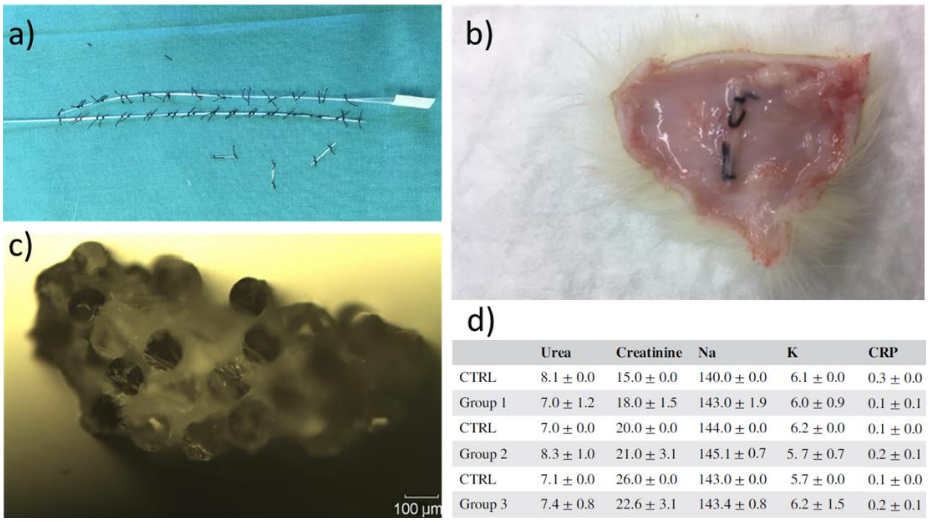

	Urea	Creatinine	Na	K	CRP
CTRL	8.1 ± 0.0	15.0 ± 0.0	140.0 ± 0.0	6.1 ± 0.0	0.3 ± 0.0
Group 1	7.0 ± 1.2	18.0 ± 1.5	143.0 ± 1.9	6.0 ± 0.9	0.1 ± 0.1
CTRL	7.0 ± 0.0	20.0 ± 0.0	144.0 ± 0.0	6.2 ± 0.0	0.1 ± 0.0
Group 2	8.3 ± 1.0	21.0 ± 3.1	145.1 ± 0.7	5. 7 ± 0.7	0.2 ± 0.1
CTRL	7.1 ± 0.0	26.0 ± 0.0	143.0 ± 0.0	5.7 ± 0.0	0.1 ± 0.0
Group 3	7.4 ± 0.8	22.6 ± 3.1	143.4 ± 0.8	6.2 ± 1.5	0.2 ± 0.1

Fig. 8. *In-vivo* test of the bioresorbable optical fibers was realized by the implantation of a a) fiber bundle in b) the subcutis of rats. The bundle removed after test is shown in c), while the blood test showing no signs of inflammation is reported in d). Adapted from [14]. Copyright ©2019 WILEY-VCH Verlag GmbH & Co.

Mild to minimal fibrosis accompanied by some bands of newly formed capillaries were found in the subcutis of both test and control animals for all the time intervals considered. In the interval of 28 and 35 days, the intensity of these lesions got milder. Furthermore, occurrence of a mild focal chronic inflammation in the subcutis was detected in some administered and one control rat. In summary, there were no significant clinical differences between test and control animals. No signs of hepatotoxicity or nephrotoxicity were found in the liver and kidneys parenchyma of the experimental animals after implantation of the bioresorbable fibers.

The results of the *in-vivo* tests show a good biocompatibility of the fibers and open up very interesting scenarios for their application in biomedicine. In the following Sections, a few of these potential applications will be reviewed.

3 Applications

3.1 Bioresorbable optical fiber Bragg grating sensors

Over the last years, optical fiber technology has attracted an ever-increasing interest in different biomedical applications, such as endoscopic imaging, localized tissue modification, and diagnostic and therapeutic sensing [15].

Focusing on biomedical sensing, one of the most promising technologies involving optical fibers is that of fiber Bragg gratings (FBGs) [16, 17]. A FBG is a type of distributed Bragg reflector constructed in a short segment of optical fiber that reflects particular wavelengths of light and transmits all others, and is achieved by creating a periodic modulation in the refractive index of the fiber core along its longitudinal direction.

During the last two decades, FBG sensors have been efficiently applied in a wide selection of biosensing applications, including articular joint pressure monitoring [18], plantar pressure and human–machine interface sensing pads [19], DNA detection [20], measuring mechanical strain in bones [21], pressure detection inside the bloodstream, and local in-vivo temperature probes [22].

Thermally durable Bragg gratings have been successfully inscribed in phosphate glass optical fibers using a variety of laser sources [23–25]. The combination of a bioresorbable phosphate glass optical fiber with Bragg grating reflectors paves the way toward new soluble photonic sensing probes with the potential characteristic of in-body operation for the efficient monitoring of vital mechanical or chemical parameters. In the following Subsections, results on the inscription of Bragg gratings into our custom-made bioresorbable phosphate glass optical fiber, using both an ultraviolet (UV) 193 nm excimer laser [26] and a visible 517 nm femtosecond (fs) laser [27], will be presented and discussed.

UV laser written FBGs through the phase-mask technique. The Bragg gratings were inscribed onto 10 cm-long bioresorbable phosphate fiber sections, previously fusion spliced to a standard single-mode (SM) fiber (SMF-28e, Corning Inc.). The inscription set-up consisted of a standard 1064.7 nm period phase-mask and a 193 nm high spatial coherence and 10 ns pulse duration excimer laser (Braggstar, TUI laser). The energy density of the inscription beam was set to 108 mJ/cm^2, as higher energy densities revealed to induce surface damage to the fiber cladding [26]. The gratings transmission and reflection spectra were real time monitored during inscription using a broadband superluminescent diode source and an optical spectrum analyzer.

A 100 min irradiation at 10 Hz resulted in the monotonous shift of the inscribed Bragg wavelength to higher values, as shown in Fig. 9a. The reflected signal strength for the first 20 min of irradiation (accumulated energy density of 1 J/cm^2) showed a linear increase, while a longer exposure to deep UV laser radiation led to saturation. A 6 dB strong notch was formed for an accumulated energy density dose of approximately 4 J/cm^2 (Fig. 9b) [26]. This grating inscription behavior is considered to be of Type I nature [24]. Based on the Bragg wavelength shift illustrated in Fig. 9a, the induced average refractive index change at the end of the inscription was found equal to 5.8×10^{-4} [16].

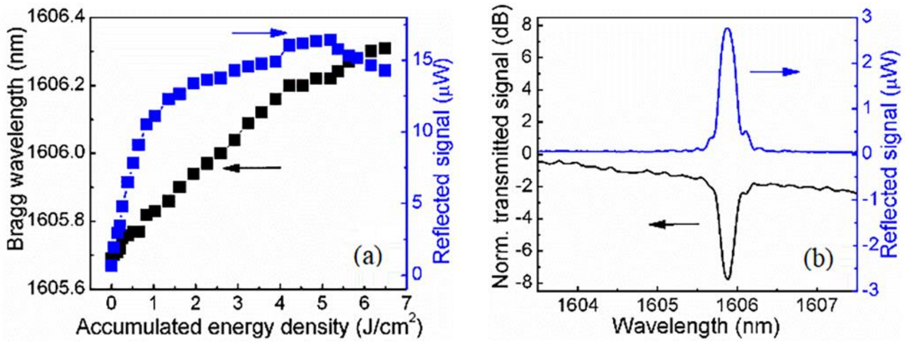

Fig. 9. (a) Bragg wavelength and reflected signal strength evolution during a 100 min inscription of a 5 mm FBG with an UV laser beam pulse energy density of 108 mJ/cm^2 and 10 Hz repetition rate. (b) Normalized transmission and reflection signals of a standard FBG after an accumulated energy density dose of 4 J/cm^2. Adapted from [26] under the Creative Common license CC BY.

In addition to the standard FBGs, tilted FBGs [28] with tilting angles equal to 1 and 0.8° were also successfully recorded [26, 29]. These gratings, taking advantage of a certain tilting angle between the grating plane and the longitudinal fiber axis, allow not only the coupling of the counter-propagating core mode, but also the coupling of the core mode to higher-order cladding modes with azimuthal field component.

For the inscription of the tilted FBGs, the phase mask holder was tilted with respect to the horizontal axis of the optical fiber. Initial grating recording attempts at a tilting angle of 2° and an exposure energy dose of 4 J/cm^2 did not result in the simultaneous inscription of measurable Bragg and cladding mode resonance signals due to the low numerical aperture (NA) of the optical fiber, thus the tilting angle was lowered to 1° or even less.

Figs. 10a and 10b show the normalized transmission signal for FBGs inscribed with tilting angles of 1° and 0.8°, respectively. The tilted FBGs were inscribed with the same UV laser beam inscription conditions employed earlier. The inscription time was 80 min for the case of 1° tilt angle and 60 min for the 0.8° one, yielding a corresponding accumulated energy density of 5.2 and 3.9 J/cm^2, respectively.

In addition to the fundamental Bragg peak attenuation signal, which is diminished in strength in comparison to the standard inscription but still present at 1606 nm, the tilted FBG spectra show the so-called “ghost” peak at 1605.3 nm. This peak has similar characteristics with the Bragg line and is ascribable to the superposition of several tightly confined lower-order cladding modes [30]. The increase of the tilting angle from 0.8 up to 1° proved to have a strong effect on the relative strength of the fundamental and “ghost” mode peaks. For the case of the 1° inscription, the suppression of the fundamental mode and the corresponding enhancement of the “ghost” one rendered the strength of the two lines almost equal. As highlighted in Figs. 10a and 10b, the spectra do not display any additional noticeable higher order cladding mode resonances at shorter wavelengths. For the case of the 1° tilting angle, an indication of smaller peaks is visible at around 1603.8 nm, which is however masked by noise features of the transmission signal.

The corresponding reflected signal of the 1° tilted FBG and its vertical zoom-up are shown in Figs. 10c and 10d; similar data were recorded for the 0.8° case (not shown here). Fig. 10d highlights the presence of a number of cladding mode peaks of smaller strength, compared to the Bragg one, at shorter wavelengths. The occurrence of those cladding modes is facilitated by the fringe recording along the whole fiber volume, which is responsible for the recoupling of a certain amount of light in the core in back propagating mode, as well as by the geometry of the splice joint (shown in the inset of Fig. 10d), that partially acts as a mirror [31].

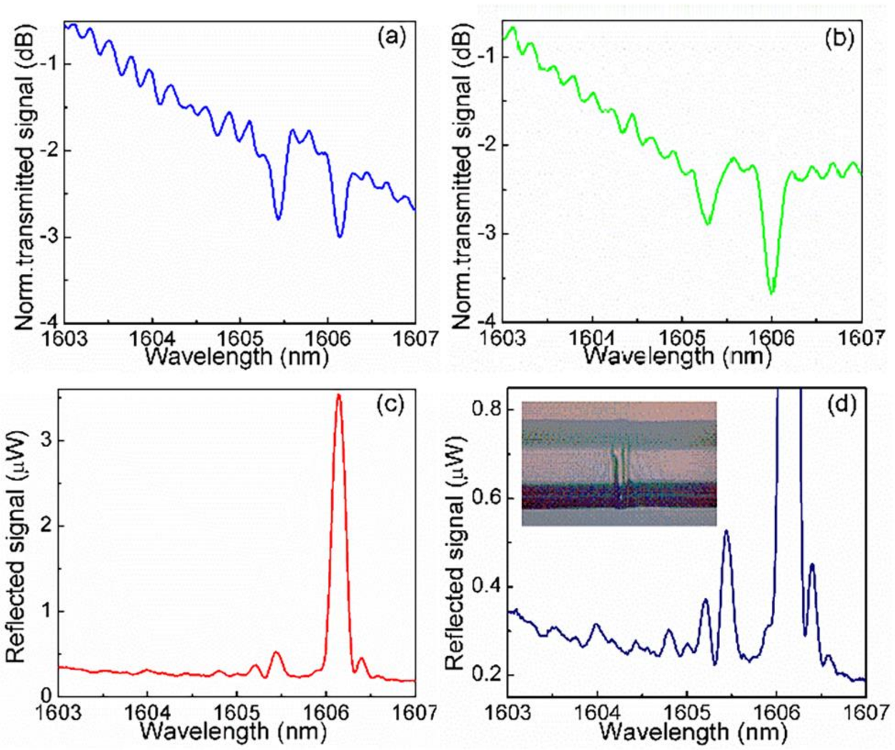

Fig. 10. Normalized transmission signal for FBGs inscribed with a phase mask tilting angle of (a) 1° and (b) 0.8°. (c) Reflected signal of the 1° tilted FBG and (d) vertical magnification of (c). The inset of (d) shows an image of the splice joint of the phosphate and SMF-28e fibers. Adapted from [26] under the Creative Common license CC BY and from [29] with permission from the Institute of Electrical and Electronics Engineers.

To allow online monitoring of the optical fiber dissolution, the 1° tilted FBG was immersed into a PBS solution at 37 °C and pH = 7.4. The evolution of the grating signal was monitored regularly up to 56 h [26], and the spectra recorded for the reflected signal are shown in Fig. 11.

It is worthwhile highlighting that changes in the reflected signal are evident just after a few hours in the solution, with the appearance of additional cladding mode peaks in the region between 1603 and 1605 nm. For prolonged immersion periods, i.e. 49 h onward, the fundamental FBG peak exhibited modifications also in wavelength, shape, and strength. In particular, a strength reduction from an initial value of 0.78 dB down to 0.25 dB was assessed after an immersion time of 56 h. This behavior is not surprising, since the "ghost" mode corresponds to low-order cladding modes characterized by a modal dispersion response that is highly similar to that of the core guiding mode manifested at the fundamental Bragg peak [28].

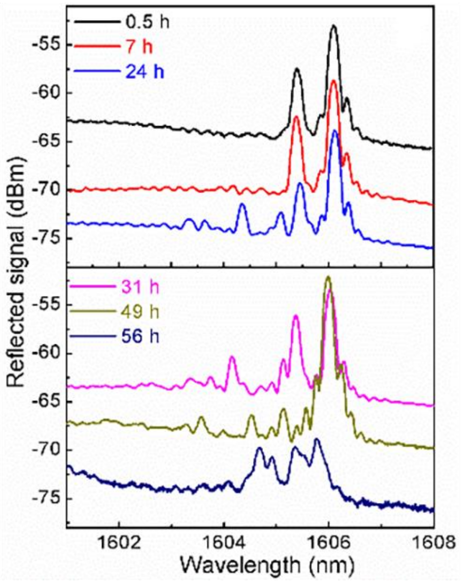

Fig. 11. Reflected signal evolution of an 1° tilted FBG immersed in PBS solution for up to 56 h. The baseline of the different spectra has been adjusted vertically to assist visualization. Adapted from [26] under the Creative Common license CC BY.

Femtosecond laser written FBGs through the plane-by-plane technique. Our in-house developed bioresorbable phosphate glass optical fiber exhibited not only a good photosensitivity to deep UV light [26], but it also proved to be suitable for fs laser processing [27]. More specifically, different types of Bragg grating-based optical filters, such as uniform FBGs, chirped gratings, and fiber Fabry-Perot (FFP) cavities, were successfully inscribed into it using a 517 nm fs laser. The direct-write plane-by-plane inscription method was selected, as it offers excellent flexibility in sensor development [32].

The Bragg grating inscription set-up consisted of a fs laser system (femtoRegen HighQ) operating at 517 nm, with 220-fs pulse duration and a nm-accuracy air-bearing translation stage system (Aerotech) for controlled and accurate two-axis motion during the inscription [33, 34]. The fiber samples were carefully mounted on the translation stage and the laser beam was focused from above using a third stage and a long working distance microscope objective (Mitutoyo, x50, NA 0.42). The pulse energy at the exit of the laser was set to 100 nJ for a laser repetition rate of 2 kHz, controlled using a pulse picker.

For the inscription of the uniform FBG operating at 1563.08 nm, the grating period (Λ) was close to 2 μm (4th order FBG) and was selected to avoid any overlapping index change. The laser was swept perpendicularly to the fiber axis generating a plane across the fiber core, and the inscription width was set to 15 μm (equal to the core diameter). The total number of periods was fixed to 1000, resulting in a ~2 mm grating length (L) [27].

Following the inscription, the bioresorbable phosphate fiber sample was fusion spliced to a standard telecom SM fiber (SMF-28e, Corning Inc.) by setting the intensity of the electric arc at a very low value and by shifting the relative position of the splicing location 700 μm towards the silica fiber.

The FBG reflection spectrum (see Fig. 12a) was then recovered using an optical spectrum analyzer (OSA) with optical resolution of 10 pm through an optical circulator, with illumination from a broadband light-source (Thorlabs ASE730). From the reflection spectrum, the bandwidth full width at half maximum (FWHM) and the effective refractive index (n_{eff}) of the grating were found to be 0.5 nm and ~ 1.515. A bright field microscope image of the inscribed grating, as captured with a charge-coupled device (CCD) camera during the inscription, is shown in Fig. 12b. The image shows the extent of the fiber diameter and the grating location, which has been designed to completely cover the core region.

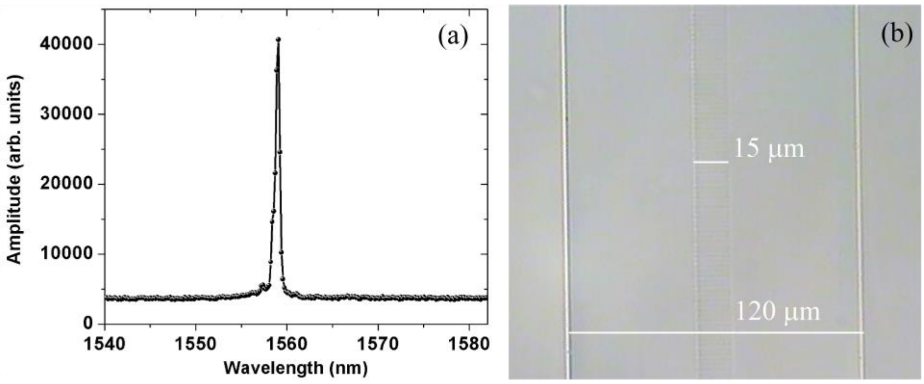

Fig. 12. (a) Reflection spectrum of a 4th order FBG inscribed in the bioresorbable phosphate fiber using the fs laser. (b) Microscope picture of the laser-induced refractive index change. Adapted from [27] with permission from the Institute of Electrical and Electronics Engineers.

The uniform 4th order FBG response to temperature and relative humidity (RH) changes was initially evaluated. To this aim, the FBG was placed in a climate chamber (Memmet 108HCP) and interrogated in reflection.

For the measurement of the temperature sensitivity, the RH of the chamber was kept constant at 35%, whereas the temperature was set to increase from 23 to 73 °C in a one-hour cycle. The temperature response of the grating was found to be 12.7 pm/°C [27], in agreement with the 10.5 pm/°C typically measured for standard single-mode optical glass fibers [16]. For the humidity tests, instead, the climate chamber temperature was kept constant at 36 °C and the RH was increased from 35 to 95%. After 4 h, the FBG wavelength shifted by only 0.025 nm, thus leading to a very low response to RH of 0.416 pm/%RH [27], as expected when dealing with a glass-based fiber.

Subsequently, the grating sample was kept for up to 52 h into the climate chamber at 95% RH; the grating exhibited a significant profile distortion and its amplitude progressively decreased, whereas the resonance wavelength of the grating shifted towards shorter wavelengths, indicating erasure.

As a further step in this research, the inscription of a chirped grating was carried out. In this case, the period of the grating was linearly increased with a chirp coefficient for each period as follows:

$$\Lambda_z = \Lambda_0 + k_z, \tag{1}$$

where Λ_0 is the initial period of the grating and k_z is the chirp coefficient for $0 < z < L$. For the 4th order FBG at 1561 nm, the initial and the final periods were ~ 2.060 and ~ 2.067 μm, respectively, corresponding to a reflection wavelength of 1566 nm and resulting in a 5 nm chirped grating (see Fig. 13a) [27]. Ripples of up to 1 dB of the maximum reflection value were observed, however they could potentially be reduced by using a smaller chirp coefficient and a higher number of periods.

Finally, an FFP cavity was inscribed using two identical FBGs with a physical separation of 3.4 mm [27]. The total cavity length must consider the light penetration depth through each grating, and so is estimated as the sum of the cavity length and approximately half of each grating length [35]. For gratings of length ~ 0.8 mm, the effective optical length of the cavity (L_{cavity}) is ~ 4.2 mm. The cavity free spectral range (FSR) is given by:

$$\lambda_{FSR} = \frac{\lambda^2}{2n_{eff}L_{cavity}}, \tag{2}$$

where λ is the light wavelength and n_{eff} is the effective refractive index. According to the FBG inscription, n_{eff} was ~ 1.515 and for gratings operating at ~ 1561 nm the FSR is approximately equal to 190 pm (see Fig. 13b). The finesse of the fiber Fabry-Perot cavity is given by:

$$finesse = \frac{\lambda_{FSR}}{\delta\lambda} = \frac{4\sqrt{R_1R_2}}{\left(1-\sqrt{R_1R_2}\right)^2}, \tag{3}$$

where $\delta\lambda$ is the FWHM of the fringes and R_1 and R_2 are the maximum reflectivity of each grating. From Eq. (3), the calculated cavity finesse is 3.16, thus indicating an average grating reflectivity of ~ 53%. The finesse and the reflectivity of the cavity could possibly be enhanced by inscribing Bragg gratings with longer length.

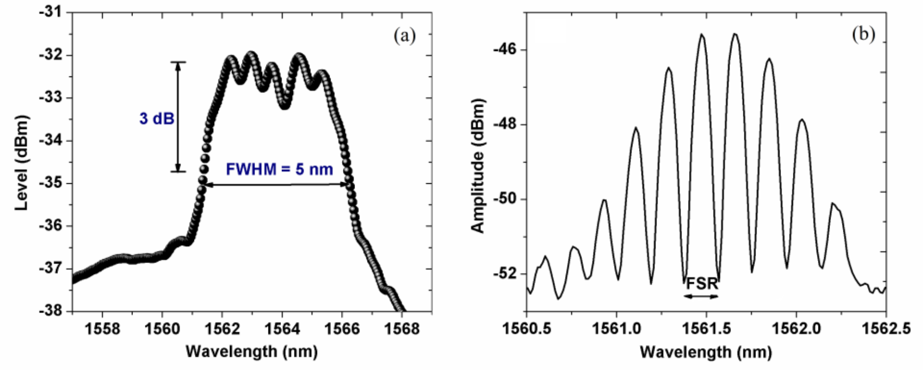

Fig. 13. Reflection spectrum of a (a) 5 nm chirped grating and a (b) Fabry-Perot cavity inscribed in the bioresorbable phosphate glass optical fiber. Adapted from [27] with permission from the Institute of Electrical and Electronics Engineers.

3.2 Time-domain diffuse optics using bioresorbable optical fibers

Diffuse optics (DO) is an attractive optical technique which aims to investigate the optical properties of a diffusive medium using light in the near-infrared spectral region, where the water absorption is negligible [36]. The most widespread application of DO is on biological tissues such as brain, muscles, breast, bones and others [37–41], for which quantitative information on tissue components (e.g. lipid, collage, water) or metabolic and oxidative state indicators (e.g. oxygen, saturation, hemoglobin and flux) can be derived. Such information can be related to the tissue regeneration, to the healing process, or to a harmful evolution.

The time-domain (TD) approach, based on the use of a picosecond pulsed laser source and time-resolved single-photon-detection, improves DO capabilities in terms of depth resolution and sensitivity [42].

The use of a phosphate bioresorbable optical fiber in diffuse optics is particularly attractive in applications where there is the need to implant an optical fiber, like photodynamic therapy (PDT) or monitoring of a post-operative healing process. In these applications the possibility to leave the fiber in place after its function is completed without the need for an explant surgery, reduces the impact on the patient and on clinical procedures.

In the following paragraphs, a study of suitability of the phosphate bioresorbable optical fiber for time-domain diffuse optics spectroscopy (TD-DOS) deep into a biological tissue will be presented. The use of the fibers was validated first on tissue-mimicking liquid phantoms and then on a more realistic environment using a chicken breast.

Suitability of bioresorbable fibers for TD measurements: phantom measurements. The experimental set-up used for this research is shown in Fig. 14. Two different pulsed laser sources were employed for the different experiments: a four-wave mixing prototype (Fianium Ltd, UK), emitting optical pulses at 820 nm at a rate of 40 MHz, and a supercontinuum laser (SuperK Extreme, NKT Photonics, Denmark) coupled to a dual-channel Acousto-Optical Tunable Filter able to provide optical pulses at 80 MHz with a wavelength tunable in the 500-1100 nm range [43].

The laser light was then attenuated using a variable optical attenuator (VOA) and delivered to the sample through a bioresorbable optical fiber (depicted in grey in Fig. 14), that was coupled to a commercial silica fiber (depicted in blue).

A second bioresorbable fiber was used to collect light from the sample and was coupled to a detector (100 µm active area diameter single-photon avalanche diode (SPAD), Micro Photon Devices Srl, Italy) through a doublet of lenses with a demagnification factor of 2.

The phosphate fibers were immersed by about 30 mm into the sample to mimic an interstitial measurement and they were spaced by 20 mm (source-detector distance, ρ).

The phosphate fibers, tailored in their composition to increase the numerical aperture (NA = 0.17 at 633 nm) so as to enhance the light harvesting, featured three different core diameters: 50, 100 and 200 µm.

Complete details of the bioresorbable fiber and of all the components of the set-up can be found in [43].

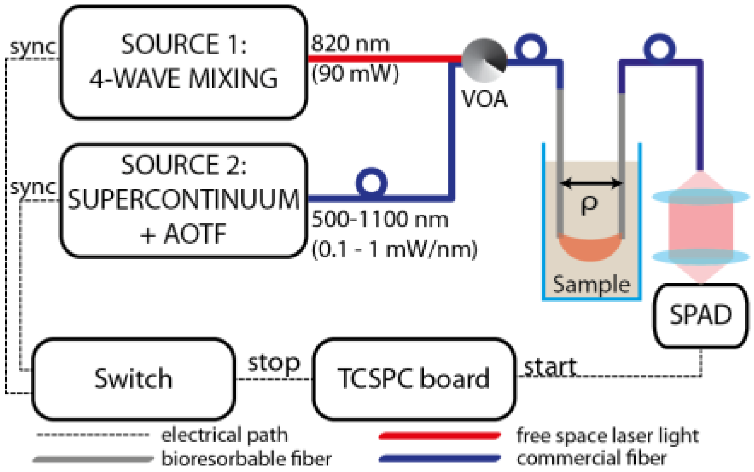

Fig. 14. Schematic of the experimental set-up. The sources 1 and 2 were used for the linearity and spectroscopy measurements, respectively. Adapted from [43].

To study the aptness of phosphate bioresorbable fibers for TD-DOS, a standardized protocol for the objective performance assessment of diffuse optics instruments was followed. At first the instrument response function (IRF), described in the basic instrumental performance (BIP) protocol [44], was measured to characterize the overall time resolution of the instrument and to assess the intrinsic suitability of the set-up for DOS measurement.

Subsequently, the linearity test, contained in the MEDPHOT protocol [45], was carried out to determine the performance of the system in retrieving the absorption (μ_a) and reduced scattering coefficients (μ'_s) of a reference homogeneous diffusive medium [46].

Figure 15 displays the IRF of the realized set-up. In Fig. 15a the IRF at 820 nm acquired using all the fibers of the set (50, 100, 200 µm) is shown, while the Fig. 15b reports the IRF at three randomly chosen wavelengths (650, 820 and 1000 nm) using the 100 µm core phosphate fiber.

The FWHM is always lower than 75 ps for all wavelengths and fiber dimensions; the dynamic range is larger than 4 decades at 820 nm, while decreases to 3 for 1000 nm. No fluorescence or backscattering from all the bioresorbable fibers tested was detected at all wavelengths, while the only exponential decay present is the diffusion tail of the SPAD, thus confirming the suitability of bioresorbable fibers for TD-DOS [46].

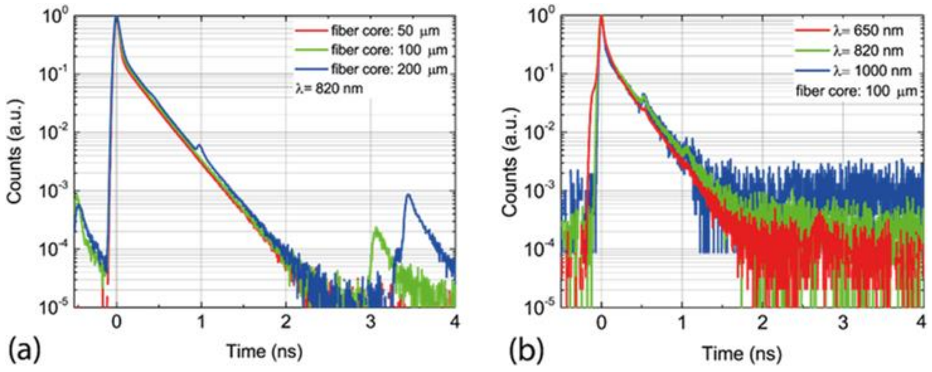

Fig. 15. (a) Instrument response functions (IRFs) acquired at 820 nm using phosphate fibers with 50, 100 and 200 µm core diameter. (b) IRFs at three randomly selected wavelengths (650, 820 and 1100 nm) acquired using the 100 µm core fiber. Reproduced from [46]. Copyright ©2017 WILEY-VCH Verlag GmbH & Co.

The linearity measurement was checked by using a liquid phantom composed of water, intralipid (providing scattering properties) and ink (acting as absorber).

By properly mixing of the above components, the desired (“true” in Fig. 16) optical properties of the phantom were obtained [47]. For this research, phantoms combining 4 values for the scattering coefficient (μ'_s = 5, 10, 15 and 20 cm^{-1} at 820 nm) with 8 values for the absorption one (μ_a ranging from 0.02 to about 0.70 cm^{-1}) were synthesized. The optical properties were then recovered by fitting the experimental measurements to an analytical model obtained under the diffusion approximation, which describes the photon transport in an infinite diffusive medium [48].

Figure 16 shows the results of linearity measurements for all set of fibers (columns) [46]. The first row reports the linearity in absorption, i.e. measured values of μ_a against the true ones. The system is linear till 0.70 cm^{-1} for the 50 μm core fiber, while the 100 and 200 μm ones show a linear behavior till 0.37 cm^{-1}. This difference is explained by the presence of a higher number of reflections in the larger core fibers, that can impair the fitting procedure.

The second and third rows of Fig. 16 show the coupling between absorption and scattering. The plots indicate a good independency between the two parameters, except for high scattering values (15 and 20 cm^{-1}) and high absorption (0.69 cm^{-1}), where the fit was not reliable as stated for the first row of the graph.

The last row of Fig. 16 displays the linearity in scattering, i.e. measured values of μ'_s against the true ones.

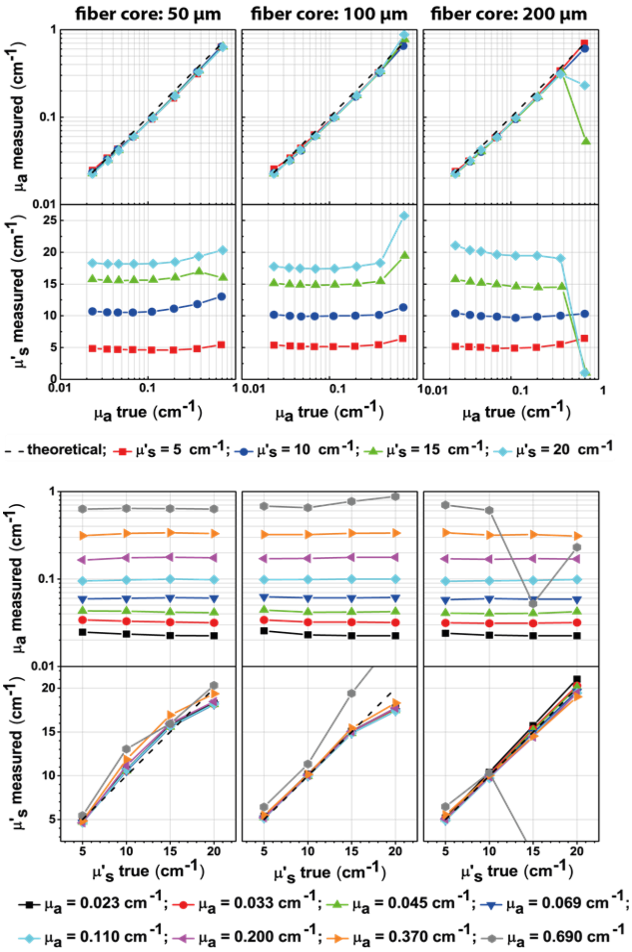

Fig. 16. Results of the linearity measurements for the three fibers under test. Reproduced from [46]. Copyright ©2017 WILEY-VCH Verlag GmbH & Co.

The behavior of the system is almost linear (relative error always lower than 20%) for the 50 and 100 μm core fibers, except for the scattering values of 20 cm^{-1}. For the 200 μm core fiber the linearity is good for all phantoms with absorption values lower than 0.69 cm^{-1} (maximum relative error of 10.3% at $\mu'_s = 5$ cm^{-1} and $\mu_a = 0.37$ cm^{-1}, otherwise always lower than 4%).

Ex-vivo spectroscopy measurements. In order to demonstrate that bioresorbable fibers can be used to recover the absorption and the scattering coefficients of a living tissue, spectroscopic measurement on a chicken breast in the range 500-1100 nm was performed [46].

For comparison, the measurement was repeated by substituting the bioresorbable fibers with standard silica glass-based ones (100 μm core, NA = 0.22 from Thorlabs GmbH, Germany), thus using a system close to a state-of-the-art clinical prototype.

Figure 17 reports the measured spectra obtained using the two different systems. The results show similar peaks and trends and the same absorption-to-scattering couplings.

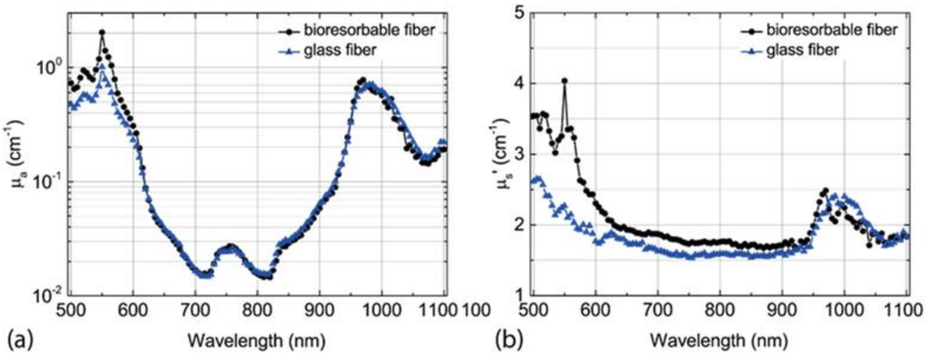

Fig. 17. Measured spectra of absorption coefficient (a) and reduced scattering (b) of a chicken breast obtained using a system based on bioresorbable fibers (black circles) and on standard glass fibers (blue triangles). Reproduced from [46]. Copyright ©2017 WILEY-VCH Verlag GmbH & Co.

The absorption spectrum is noisier around the water peak (at 970 nm) for the bioresorbable fiber, while tends to be overestimated below 600 nm, where the deoxyhemoglobin peak is located (550 nm). In both spectral regions, a low signal using the bioresorbable fiber was obtained due to high absorption.

The retrieved scattering coefficient was slightly higher (around 10%) in the “safe” 600-900 nm region for the bioresorbable fibers. The difference between the reduced scattering exhibited by the bioresorbable and standard fibers was more pronounced below 600 nm, thus in a region where low signal and absorption coupling make the scattering measurement quite unreliable.

All these measurements validated the use of phosphate bioresorbable fibers for TD-DOS and pave the way for a new generation of minimally invasive biomedical devices.

4 Future developments

The development of optically transparent resorbable phosphate glasses paves the way toward the realization of a new generation of optical fiber-based devices for biophotonics.

Beyond the examples reported in this study, bioresorbable devices might be used in other specific applications, where minimally invasive procedures including drug delivery and light assisted processes are required. These may consist for instance in developing customized probes for metronomic photodynamic therapy [49], where the bioresorbable multifunctional fiber device could help minimizing the impact of the therapy on the patient and resulting in no need of explant surgery for removing the probe.

References

1. Vogel, W.: Glass chemistry. 1st ed. Springer-Verlag, Berlin (1994).
2. Sales, B.C, Boatner, L.A.: Lead–iron phosphate glass: a stable storage medium for high–level nuclear waste. Science 226(4670), 45–48 (1984).
3. Kreidl, N.J, Weyl, W.A.: Phosphates in ceramic ware: IV, phosphate glasses. Journal of the American Ceramic Society 24(11), 372–378 (1941).
4. Campbell, J.H, Hayden, J.S, Marker, A.: High-power solid-state lasers: a laser glass perspective. International Journal of Applied Glass Science 2(1), 3–29 (2011).
5. Boetti, N.G., Pugliese, D., Ceci-Ginistrelli, E., Lousteau, J., Janner, D., Milanese, D.: Highly doped phosphate glass fibers for compact lasers and amplifiers: a review. Applied Sciences 7(12), 1295 (2017).
6. http://www.npphotonics.com/products, last accessed 2020/12/06.
7. Abou Neel, E.A., Chrzanowski, W., Knowles, J.C.: Effect of increasing titanium dioxide content on bulk and surface properties of phosphate-based glasses. Acta Biomaterialia 4(3), 523–534 (2008).
8. Ahmed, I., Jones, I.A., Parsons, A.J., Bernard, J., Farmer, J., Scotchford, C.A., Walker, G.S., Rudd, C.D.: Composites for bone repair: phosphate glass fibre reinforced PLA with varying fibre architecture. Journal of Materials Science: Materials in Medicine 22, 1825–1834 (2011).
9. Vitale-Brovarone, C., Novajra, G., Lousteau, J., Milanese, D., Raimondo, S., Fornaro, M.: Phosphate glass fibres and their role in neuronal polarization and axonal growth direction. Acta Biomaterialia 8(3), 1125–1136 (2012).
10. Ceci-Ginistrelli, E., Pugliese, D., Boetti, N.G., Novajra, G., Ambrosone, A., Lousteau, J., Vitale-Brovarone, C., Abrate, S., Milanese, D.: Novel biocompatible and resorbable UV-transparent phosphate glass based optical fiber. Optical Materials Express 6(6), 2040–2051 (2016).

11. Gallichi-Nottiani, D., Pugliese, D., Boetti, N.G., Milanese, D., Janner, D.: Toward the fabrication of extruded microstructured bioresorbable phosphate glass optical fibers. International Journal of Applied Glass Science 11(4), 632–640 (2020).
12. Boetti, N.G., Ceci-Ginistrelli, E., Pugliese, D., Novajra, G., Vitale-Brovarone, C., Lousteau, J., Abrate, S., Milanese, D.: Bioresorbable calcium-phosphate optical fiber. In: Proceedings Advanced Photonics 2016, p. 1. Optical Society of America, Vancouver, Canada (2016).
13. Sglavo, V.M., Pugliese, D., Sartori, F., Boetti, N.G., Ceci-Ginistrelli, E., Franco, G., Milanese, D.: Mechanical properties of resorbable calcium-phosphate glass optical fiber and capillaries. Journal of Alloys and Compounds 778, 410–417 (2019).
14. Podrazký, O., Peterka, P., Kašík, I., Vytykáčová, S., Proboštová, J., Mrázek, J., Kuneš, M., Závalová, V., Radochová, V., Lyutakov, O., Ceci-Ginistrelli, E., Pugliese, D., Boetti, N.G., Janner, D., Milanese, D.: In vivo testing of a bioresorbable phosphate-based optical fiber. Journal of Biophotonics 12(7), e201800397 (2019).
15. Chin, L.C.L., Whelan, W.M., Vitkin, I.A.: Optical-thermal response of laser-irradiated tissue. 2nd edn. Springer, Heidelberg (2011).
16. Othonos, A., Kalli, K.: Fiber Bragg gratings: fundamentals and applications in telecommunications and sensing. 1st edn. Artech House, Boston (1999).
17. Berghmans, F., Geernaert, T., Baghdasaryan, T., Thienpont, H.: Challenges in the fabrication of fibre Bragg gratings in silica and polymer microstructured optical fibres. Laser & Photonics Reviews 8(1), 27–52 (2014).
18. Dennison, C.R., Wild, P.M., Wilson, D.R., Gilbart, M.K.: An in-fiber Bragg grating sensor for contact force and stress measurements in articular joints. Measurement Science and Technology 21(11), 115803 (2010).
19. Candiani, A., Konstantaki, M., Pamvouxoglou, A., Pissadakis, S.: A shear sensing pad, based on ferrofluidic actuation in a microstructured optical fiber. IEEE Journal of Selected Topics in Quantum Electronics 23(2), 210–216 (2017).
20. Bertucci, A., Manicardi, A., Candiani, A., Giannetti, S., Cucinotta, A., Spoto, G., Konstantaki, M., Pissadakis, S., Selleri, S., Corradini, R.: Detection of unamplified genomic DNA by a PNA-based microstructured optical fiber (MOF) Bragg-grating optofluidic system. Biosensors and Bioelectronics 63, 248–254 (2015).
21. Carvalho, L., Alberto, N.J., Gomes, P.S., Nogueira, R.N., Pinto, J.L., Fernandes, M.H.: In the trail of a new bio-sensor for measuring strain in bone: Osteoblastic biocompatibility. Biosensors and Bioelectronics 26(10), 4046–4052 (2011).
22. Favero, F.C., Pruneri, V., Villatoro, J.: Microstructured optical fiber interferometric breathing sensor. Journal of Biomedical Optics 17(3), 037006 (2012).
23. Grobnic, D., Mihailov, S.J., Walker, R.B., Smelser, C.W., Lafond, C., Croteau, A.: Bragg gratings made with a femtosecond laser in heavily doped Er–Yb phosphate glass fiber. IEEE Photonics Technology Letters 19(12), 943–945 (2007).
24. Albert, J., Schülzgen, A., Temyanko, V.L., Honkanen, S., Peyghambarian, N.: Strong Bragg gratings in phosphate glass single mode fiber. Applied Physics Letters 89(10), 101127 (2006).
25. Sozzi, M., Rahman, A., Pissadakis, S.: Non-monotonous refractive index changes recorded in a phosphate glass optical fibre using 248nm, 500fs laser radiation. Optical Materials Express 1(1), 121–127 (2011).
26. Pugliese, D., Konstantaki, M., Konidakis, I., Ceci-Ginistrelli, E., Boetti, N.G., Milanese, D., Pissadakis, S.: Bioresorbable optical fiber Bragg gratings. Optics Letters 43(4), 671–674 (2018).

27. Theodosiou, A., Pugliese, D., Ceci-Ginistrelli, E., Boetti, N.G., Janner, D., Milanese, D., Kalli, K.: Femtosecond laser written plane-by-plane Bragg grating sensors in bioresorbable phosphate optical fibres. Journal of Lightwave Technology 37(10), 2363–2369 (2019).
28. Albert, J., Shao, L.-Y., Caucheteur, C.: Tilted fiber Bragg grating sensors. Laser & Photonics Reviews 7(1), 83–108 (2013).
29. Konstantaki, M., Pissadakis, S., Pugliese, D., Ceci-Ginistrelli, E., Boetti, N.G., Milanese, D.: Bragg grating UV inscription in a bioresorbable phosphate glass optical fiber. In: 18th International Conference on Transparent Optical Networks (ICTON), pp. 1–4. Institute of Electrical and Electronics Engineers, Trento, Italy (2016).
30. Poulsen, T., Berendt, O., Bjarklev, A., Gruner-Nielsen, L., Soccolich, C.E.: Bragg grating induced cladding mode coupling caused by ultra-violet light absorption. Electronics Letters 34(10), 1007–1009 (1998).
31. Chan, C.-F., Chen, C., Jafari, A., Laronche, A., Thomson, D.J., Albert, J.: Optical fiber refractometer using narrowband cladding-mode resonance shifts. Applied Optics 46(7), 1142–1149 (2007).
32. Theodosiou, A., Lacraz, A., Polis, M., Kalli, K., Tsangari, M., Stassis, A., Komodromos, M.: Modified fs-laser inscribed FBG array for rapid mode shape capture of free-free vibrating beams. IEEE Photonics Technology Letters 28(14), 1509–1512 (2016).
33. Fokine, M., Theodosiou, A., Song, S., Hawkins, T., Ballato, J., Kalli, K., Gibson, U.J.: Laser structuring, stress modification and Bragg grating inscription in silicon-core glass fibers. Optical Materials Express 7(5), 1589–1597 (2017).
34. Theodosiou, A., Hu, X., Caucheteur, C., Kalli, K.: Bragg gratings and Fabry-Perot cavities in low-loss multimode CYTOP polymer fiber. IEEE Photonics Technology Letters 30(9), 857–860 (2018).
35. Barmenkov, Y.O., Zalvidea, D., Torres-Peiró, S., Cruz, J.L., Andrés, M.V.: Effective length of short Fabry-Perot cavity formed by uniform fiber Bragg gratings. Optics Express 14(14), 6394–6399 (2006).
36. Gibson, A.P., Hebden, J.C., Arridge, S.R.: Recent advances in diffuse optical imaging. Physics in Medicine & Biology 50(4), R1–R43 (2015).
37. Durduran, T., Choe, R., Baker, W.B., Yodh, A.G.: Diffuse optics for tissue monitoring and tomography. Reports on Progress in Physics 73(7), 076701 (2010).
38. Bashkatov, A.N., Genina, E.A., Tuchin, V.V.: Optical properties of skin, subcutaneous, and muscle tissues: A review. Journal of Innovative Optical Health Sciences 4(1), 9–38 (2011).
39. Torricelli, A., Contini, D., Dalla Mora, A., Pifferi, A., Re, R., Zucchelli, L., Cani, M., Farina, A., Spinelli, L.: Neurophotonics: non-invasive optical techniques for monitoring brain functions. Functional Neurology 29(4), 223–230 (2014).
40. Hoshi, Y., Yamada, Y.: Overview of diffuse optical tomography and its clinical applications. Journal of Biomedical Optics 21(9), 091312 (2016).
41. Lange, F., Tachtsidis, I.: Clinical brain monitoring with time domain NIRS: A review and future perspectives. Applied Sciences 9(8), 1612 (2019).
42. Dalla Mora, A., Di Sieno, L., Re, R., Pifferi, A., Contini, D.: Time-gated single-photon detection in time-domain diffuse optics: A review. Applied Sciences 10(3), 1101 (2020).
43. Di Sieno, L., Boetti, N.G., Dalla Mora, A., Pugliese, D., Farina, A., Konugolu Venkata Sekar, S., Ceci-Ginistrelli, E., Janner, D., Pifferi, A., Milanese, D.: Time-domain diffuse optics using bioresorbable fibers: a proof-of-principle study. In: Amelink, A., Vitkin, I.A. (eds.) European Conference on Biomedical Optics 2017, Novel Biophotonics Techniques and Applications IV, vol. 10413, pp. 1–5. Optical Society of America-Society of Photo-Optical Instrumentation Engineers, Washington-Bellingham, USA (2017).

44. Wabnitz, H., Taubert, D.R., Mazurenka, M., Steinkellner, O., Jelzow, A., Macdonald, R., Milej, D., Sawosz, P., Kacprzak, M., Liebert, A., Cooper, R., Hebden, J., Pifferi, A., Farina, A., Bargigia, I., Contini, D., Caffini, M., Zucchelli, L., Spinelli, L., Cubeddu, R., Torricelli, A.: Performance assessment of time-domain optical brain imagers, part 1: basic instrumental performance protocol. Journal of Biomedical Optics 19(8),086010 (2014).
45. Pifferi, A., Torricelli, A., Bassi, A., Taroni, P., Cubeddu, R., Wabnitz, H., Grosenick, D., Möller, M., Macdonald, R., Swartling, J., Svensson, T., Andersson-Engels, S., van Veen, R.L.P., Sterenborg, H.J.C.M., Tualle, J.-M., Nghiem, H.L., Avrillier, S., Whelan, M., Stamm, H.: Performance assessment of photon migration instruments: the MEDPHOT protocol. Applied Optics 44(11), 2104–2114 (2005).
46. Di Sieno, L., Boetti, N.G., Dalla Mora, A., Pugliese, D., Farina, A., Konugolu Venkata Sekar, S., Ceci-Ginistrelli, E., Janner, D., Pifferi, A., Milanese, D.: Towards the use of bioresorbable fibers in time-domain diffuse optics. Journal of Biophotonics 11(1), e201600275 (2018).
47. Spinelli, L., Botwicz, M., Zolek, N., Kacprzak, M., Milej, D., Sawosz, P., Liebert, A., Weigel, U., Durduran, T., Foschum, F., Kienle, A., Baribeau, F., Leclair, S., Bouchard, J.-P., Noiseux, I., Gallant, P., Mermut, O., Farina, A., Pifferi, A., Torricelli, A., Cubeddu, R., Ho, H.-C., Mazurenka, M., Wabnitz, H., Klauenberg, K., Bodnar, O., Elster, C., Bénazech-Lavoué, M., Bérubé-Lauzière, Y., Lesage, F., Khoptyar, D., Subash, A.A., Andersson-Engels, S., Di Ninni, P., Martelli, F., Zaccanti, G.: Determination of reference values for optical properties of liquid phantoms based on Intralipid and India ink. Biomedical Optics Express 5(7), 2037–2053 (2014).
48. Contini, D., Martelli, F., Zaccanti, G.: Photon migration through a turbid slab described by a model based on diffusion approximation. I. Theory. Applied Optics 36(19), 4587–4599 (1997).
49. Bisland, S.K., Lilge, L., Lin, A., Rusnov, R., Wilson, B.C.: Metronomic photodynamic therapy as a new paradigm for photodynamic therapy: rationale and preclinical evaluation of technical feasibility for treating malignant brain tumors. Photochemistry and Photobiology 80(1), 22–30 (2004).